PHYSICAL REVIEW D **79,** 035006 (2009)

Technicolor walks at the LHC

Alexander Belyaev*

NExT Institute: School of Physics & Astronomy, University of Southampton, Highfield, Southampton SO17 1BJ, United Kingdom, and Particle Physics Department, Rutherford Appleton Laboratory, Chilton, Didcot, Oxon OX11 0QX, United Kingdom

Roshan Foadi,† Mads T. Frandsen,‡ Matti Järvinen,§ and Francesco Sannino‖

High Energy Physics Center, University of Southern Denmark, Campusvej 55, DK-5230 Odense M, Denmark

Alexander Pukhov¶

Skobeltsyn Institute of Nuclear Physics, Moscow State University, Moscow 119992, Russia

(Received 1 October 2008; published 10 February 2009)

We analyze the potential of the Large Hadron Collider (LHC) to observe signatures of phenomenologically viable walking technicolor models. We study and compare the Drell-Yan and vector boson fusion mechanisms for the production of composite heavy vectors. We find that the heavy vectors are most easily produced and detected via the Drell-Yan processes. The composite Higgs phenomenology is also studied. If technicolor walks at the LHC, its footprints will be visible and our analysis will help in uncovering them.

DOI: 10.1103/PhysRevD.79.035006 PACS numbers: 12.10.Dm

I. INTRODUCTION

Dynamical electroweak symmetry breaking (DEWSB) has a fair chance to constitute the correct extension of the standard model (SM). However, electroweak precision data (EWPD) and constraints from flavor-changing neutral currents (FCNC) both disfavor underlying gauge dynamics resembling too closely a scaled-up version of quantum chromodynamics (QCD) (see [1,2] for recent reviews). With QCD-like dynamics ruled out, what kind of four-dimensional gauge theory can be a realistic candidate for DEWSB?

Based on recent progress [1,3–7] in the understanding of walking technicolor (WT) dynamics [8–11] various phenomenologically viable models have been proposed. Primary examples are: i) the SU(2) theory with two technifavors in the adjoint representation, known as minimal walking technicolor (MWT); ii) the SU(3) theory with two flavors in the two-index symmetric representation which is called next-to-minimal walking technicolor (NMWT). These gauge theories have remarkable properties [3–7,12] and alleviate the tension with the EWPD when used for DEWSB [3,7,13,14]. First principle lattice simulations have already started [15–19] giving preliminary support to the claim that these theories are indeed (near) conformal. The finite temperature properties of these models have been recently studied in [20] in connection with the order of the electroweak phase transition.

We focus the present analysis on NMWT since this theory possesses the simplest global symmetry $(SU(2)_L \times SU(2)_R)$ yielding fewer composite particles than MWT (with its SU(4) global symmetry) [21]. Following our construction in Ref. [13] we provide a comprehensive Lagrangian for this model. Key ingredients are (i) the global symmetries of the underlying gauge theory, (ii) vector meson dominance, (iii) walking dynamics, and (iv) the ''minimality'' of the theory, that is the small number of flavors and thus a small S parameter. Based on (i) and (ii) we use for the low-energy physics a chiral resonance model containing spin zero and spin one fields. Some of the coefficients of the corresponding Lagrangian are then constrained using (iii) and (iv) through the modified Weinberg's sum rules (WSR's) [22]. Given that we cannot compute the entire set of the coefficients of the effective Lagrangian directly from the underlying gauge theory we use the practical approach of studying the various LHC observables for different values of the unknown parameters. In this respect our low-energy theory can also be seen as a template for any strongly coupled theory which may emerge at the LHC. An analysis of unitarity of the longitudinal WW vector boson scattering versus precision measurements, within the effective Lagrangian approach, can be found in Ref. [23], and shows that it is possible to pass the precision tests while simultaneously delay the onset of unitarity violation.

Clean signatures of the NMWT model come from the production of spin one resonances and the composite Higgs, followed by their decays to SM fields. In particular in this work we focus on Drell-Yan (DY) and vector boson fusion (VBF) production of the vector resonances. We also study the associate Higgs production together with a W or a Z boson. This channel is interesting due to the interplay

*a.belyaev@phys.soton.ac.uk
†roshan@fysik.sdu.dk
‡toudal@nbi.dk
§mjarvine@ifk.sdu.dk
‖sannino@ifk.sdu.dk
¶pukhov@lapp.in2p3.fr

among the SM gauge bosons, the heavy vectors and the composite Higgs.

In Sec. II we introduce the model and impose constraints on its parameter space from the LEP and Tevatron. We also use information from the underlying gauge dynamics in the form of the generalized WSRs. The LHC phenomenology is studied in Sec. III. More specifically we investigate the heavy vector production as well as the associate composite Higgs production. We summarize our results in Sec. IV.

II. THE SIMPLEST MODEL OF WALKING TECHNICOLOR

We have explained that NMWT has the simplest chiral symmetry, $\mathrm{SU}(2)_\mathrm{L} \times \mathrm{SU}(2)_\mathrm{R}$, since it is expected to be near walking with just two Dirac flavors. The low-energy description of this model can be encoded in a chiral Lagrangian including spin one resonances. Following Refs. [13,24] we write:

$$\begin{aligned}\mathcal{L}_{\mathrm{boson}} = & -\frac{1}{2}\mathrm{Tr}[\tilde{W}_{\mu\nu}\tilde{W}^{\mu\nu}] - \frac{1}{4}\tilde{B}_{\mu\nu}\tilde{B}^{\mu\nu} - \frac{1}{2}\mathrm{Tr}[F_{\mathrm{L}\mu\nu}F_{\mathrm{L}}^{\mu\nu} + F_{\mathrm{R}\mu\nu}F_{\mathrm{R}}^{\mu\nu}] + m^2\,\mathrm{Tr}[C_{\mathrm{L}\mu}^2 + C_{\mathrm{R}\mu}^2] + \frac{1}{2}\mathrm{Tr}[D_\mu M D^\mu M^\dagger] \\ & - \tilde{g}^2 r_2\,\mathrm{Tr}[C_{\mathrm{L}\mu} M C_{\mathrm{R}}^\mu M^\dagger] - \frac{i\tilde{g}r_3}{4}\mathrm{Tr}[C_{\mathrm{L}\mu}(MD^\mu M^\dagger - D^\mu M M^\dagger) + C_{\mathrm{R}\mu}(M^\dagger D^\mu M - D^\mu M^\dagger M)] \\ & + \frac{\tilde{g}^2 s}{4}\mathrm{Tr}[C_{\mathrm{L}\mu}^2 + C_{\mathrm{R}\mu}^2]\mathrm{Tr}[MM^\dagger] + \frac{\mu^2}{2}\mathrm{Tr}[MM^\dagger] - \frac{\lambda}{4}\mathrm{Tr}[MM^\dagger]^2 \end{aligned} \tag{1}$$

where $\tilde{W}_{\mu\nu}$ and $\tilde{B}_{\mu\nu}$ are the ordinary electroweak field strength tensors, $F_{\mathrm{L/R}\mu\nu}$ are the field strength tensors associated to the vector meson fields $A_{\mathrm{L/R}\mu}$ [25], and the $C_{\mathrm{L}\mu}$ and $C_{\mathrm{R}\mu}$ fields are

$$C_{\mathrm{L}\mu} \equiv A_{\mathrm{L}\mu} - \frac{g}{\tilde{g}}\tilde{W}_\mu, \qquad C_{\mathrm{R}\mu} \equiv A_{\mathrm{R}\mu} - \frac{g'}{\tilde{g}}\tilde{B}_\mu. \tag{2}$$

The 2×2 matrix M is

$$M = \frac{1}{\sqrt{2}}[v + H + 2i\pi^a T^a], \qquad a = 1, 2, 3 \tag{3}$$

where π^a are the Goldstone bosons produced in the chiral symmetry breaking, $v = \mu/\sqrt{\lambda}$ is the corresponding vacuum expectation value (VEV), H is the composite Higgs, and $T^a = \sigma^a/2$, where σ^a are the Pauli matrices. The covariant derivative is

$$D_\mu M = \partial_\mu M - ig\tilde{W}_\mu^a T^a M + ig' M \tilde{B}_\mu T^3. \tag{4}$$

When M acquires its VEV, the Lagrangian of Eq. (1) contains mixing matrices for the spin one fields. The mass eigenstates are the ordinary SM bosons, and two triplets of heavy mesons, of which the lighter (heavier) ones are denoted by $R_1^\pm$ ($R_2^\pm$) and R_1^0 (R_2^0). These heavy mesons are the only new particles, at low energy, relative to the SM.

Some remarks should be made about the Lagrangian of Eq. (1). First, the new strong interaction preserves parity, which implies invariance under the transformation

$$M \leftrightarrow M^\dagger, \qquad C_\mathrm{L} \leftrightarrow C_\mathrm{R}. \tag{5}$$

Second, we have written the Lagrangian in a "mixed" gauge. As explained in the appendix of Ref. [13], the Lagrangian for this model can be rewritten by interpreting the vector meson fields as gauge fields of a "mirror" gauge group $\mathrm{SU}(2)'_\mathrm{L} \times \mathrm{SU}(2)'_\mathrm{R}$. This is equivalent to the idea of hidden local symmetry [26,27], used in a similar context for the BESS models [28]. In Eq. (1) the vector mesons have already absorbed the corresponding pions, while the $\mathrm{SU}(2) \times \mathrm{U}(1)$ gauge fields are still transverse. Finally, Eq. (1) contains all $\mathcal{O}(p^2)$ operators of dimension two and four.

Now we must couple the SM fermions. The interactions with the Higgs and the spin one mesons are mediated by an unknown ETC sector, and can be parametrized at low energy by Yukawa terms, and mixing terms with the C_L and C_R fields. Assuming that the ETC interactions preserve parity, the most general form for the quark Lagrangian is [29]

$$\begin{aligned}\mathcal{L}_{\mathrm{quark}} = & \bar{q}_L^i i\not{D} q_{iL} + \bar{q}_R^i i\not{D} q_{iR} + \tilde{g}\bar{q}_L^i K_i^j \not{C}_\mathrm{L} q_{jL} \\ & + \tilde{g}\bar{q}_R^i K_\mathrm{R}^j q_{jR} - \left[\bar{q}_L^i (Y_u)_i^j M \frac{1+\tau^3}{2} q_{jR}\right. \\ & \left. + \bar{q}_L^i (Y_d)_i^j M \frac{1-\tau^3}{2} q_{jR} + \mathrm{H.c.}\right], \end{aligned} \tag{6}$$

where i and j are generation indices, $i = 1, 2, 3$, $q_{iL/R}$ are electroweak doublets, K is a 3×3 Hermitian matrix, and Y_u and Y_d are 3×3 complex matrices. The covariant derivatives are the ordinary electroweak ones,

$$\begin{aligned}\not{D} q_{iL} &= (\not{\partial} - ig^a T^a - ig'\tilde{\not{B}} Y_\mathrm{L}) q_{iL}, \\ \not{D} q_{iR} &= (\not{\partial} - ig'\tilde{\not{B}} Y_\mathrm{R}) q_{iR}, \end{aligned} \tag{7}$$

where $Y_\mathrm{L} = 1/6$ and $Y_\mathrm{R} = \mathrm{diag}(2/3, -1/3)$. One can exploit the global symmetries of the kinetic and K-terms to reduce the number of physical parameters in the Yukawa matrices. Thus we can take

$$Y_u = \mathrm{diag}(y_u, y_c, y_t), \qquad Y_d = V\mathrm{diag}(y_d, y_s, y_b), \tag{8}$$

and

$$q_L^i = \begin{pmatrix} u_{iL} \\ V_i^j d_{jL} \end{pmatrix}, \qquad q_R^i = \begin{pmatrix} u_{iR} \\ d_{iR} \end{pmatrix}, \tag{9}$$

where V is the Cabibbo-Kobayashi-Maskawa matrix. In principle one could also have a mixing matrix for the right-handed fields, due to the presence of the K-terms. However at this point this is an unnecessary complication, and we set this mixing matrix equal to the identity matrix. Finally, we also set

$$K = \kappa \mathbf{1}_{3\times 3}, \tag{10}$$

to prevent flavor-changing neutral currents (FCNC) to show up at tree-level. A more precise approach would require taking the experimental bounds on FCNC and using these to constrain $K - \kappa \mathbf{1}_{3\times 3}$.

A. Weinberg sum rules

In its general form Eq. (1) describes any model of DEWSB with a spontaneously broken $\mathrm{SU}(2)_\mathrm{L} \times \mathrm{SU}(2)_\mathrm{R}$ chiral symmetry. In order to make contact with the underlying gauge theory, and discriminate between different classes of models, we make use of the WSRs. In Ref. [22] it was argued that the zeroth WSR—which is nothing but the definition of the S parameter—

$$S = 4\pi\left[\frac{F_V^2}{M_V^2} - \frac{F_A^2}{M_A^2}\right], \tag{11}$$

and the first WSR,

$$F_V^2 - F_A^2 = F_\pi^2, \tag{12}$$

do not receive significant contributions from the near conformal region, and are therefore unaffected. In these equations M_V (M_A) and F_V (F_A) are mass and decay constant of the vector-vector (axial-vector) meson, respectively, in the limit of zero electroweak gauge couplings. F_π is the decay constant of the pions: since this is a model of DEWSB, $F_\pi = 246$ GeV. The Lagrangian of Eq. (1) gives

$$M_V^2 = m^2 + \frac{\tilde{g}^2(s - r_2)v^2}{4} \qquad M_A^2 = m^2 + \frac{\tilde{g}^2(s + r_2)v^2}{4}, \tag{13}$$

and

$$F_V = \frac{\sqrt{2}M_V}{\tilde{g}}, \qquad F_A = \frac{\sqrt{2}M_A}{\tilde{g}}\chi, \qquad F_\pi^2 = (1 + 2\omega)F_V^2 - F_A^2, \tag{14}$$

where

$$\omega \equiv \frac{v^2\tilde{g}^2}{4M_V^2}(1 + r_2 - r_3), \qquad \chi \equiv 1 - \frac{v^2\tilde{g}^2 r_3}{4M_A^2}. \tag{15}$$

Then Eqs. (11) and (12) give

$$S = \frac{8\pi}{\tilde{g}^2}(1 - \chi^2), \tag{16}$$

$$r_2 = r_3 - 1. \tag{17}$$

The second WSR does receive important contributions from the near conformal region, and is modified to

$$F_V^2 M_V^2 - F_A^2 M_A^2 = a\frac{8\pi^2}{d(R)}F_\pi^4, \tag{18}$$

where a is expected to be positive and $\mathcal{O}(1)$, and $d(R)$ is the dimension of the representation of the underlying fermions [22]. For each of these sum rules a more general spectrum would involve a sum over vector and axial states.

In the effective Lagrangian we codify the walking behavior in a being positive and $\mathcal{O}(1)$, and the minimality of the theory in S being small. A small S is both due to the small number of flavors in the underlying theory and to the near conformal dynamics, which reduces the contribution to S relative to a running theory [22,30,31]. In NMWT (three colors in the two-index symmetric representation) the naive one-loop S parameter is $S = 1/\pi \simeq 0.3$: this is a reasonable input for S in Eq. (11).

Figure 1 displays a contour plot of a in the $(M_A, \tilde{g})$ plane for $S = 0.3$, in NMWT ($d(\mathrm{R}) = 6$). This plot is obtained after imposing Eqs. (11) and (12). Notice that $a = \mathcal{O}(1)$ for a large portion of the parameter space, since the maximum value of a is found to be $a_{\max} = d(\mathrm{R})/(2\pi S)$, and this gives 3.18 for $S = 0.3$ and $d(\mathrm{R}) = 6$. The running regime, $a = 0$, is only attained for large values of M_A. However walking regimes, $a = \mathcal{O}(1)$, are also compatible with smaller values of M_A. For example, if we require $1 < a < 2$ with $S = 0.3$ in NMWT, from Fig 1, we see that this is both possible for $M_A \gtrsim 2.0$ TeV and $M_A \lesssim 1.0$ TeV. Although a walking regime with large values of M_A is more plausible, since this is more naturally achieved by moving away from a running regime, a walking scenario with small values of M_A cannot be excluded based solely on the WSRs analysis.

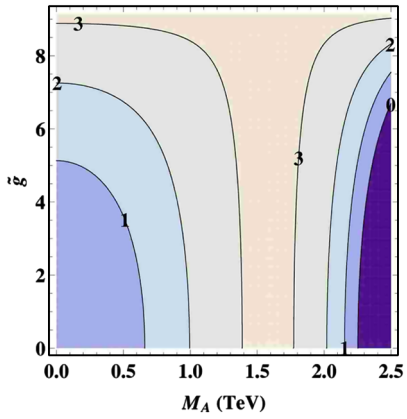

FIG. 1 (color online). Contour plot for a in the $(M_A, \tilde{g})$ plane, for $S = 0.3$ in NMWT ($d(\mathrm{R}) = 6$). We plot contours for $a = 0$, 1, 2, 3, and $3 \leq a \leq a_{\max} = d(\mathrm{R})/(2\pi S) \simeq 3.18$ (central region). The running regime corresponds to the $a = 0$ contour, which is on the lower right of the parameter space. Walking dynamics requires $a = \mathcal{O}(1) > 0$, which is achieved for a large portion of the parameter space.

B. Electroweak parameters

If the κ parameter of Eq. (10) is negligibly small, then the fermion Lagrangian of Eq. (6) describes a "universal" theory, in the sense that all the corrections to the electroweak observables show up in gauge current correlators. If this is the case the new physics effect on the low-energy observables are fully accounted for by the Barbieri *et. al.* parameters [32]. In our model these are

$$\hat{S} = \frac{g^2(1-\chi^2)}{2\tilde{g}^2 + g^2(1+\chi^2)}, \qquad \hat{T} = 0,$$
$$W = M_W^2 \frac{g^2(M_A^2 + M_V^2\chi^2)}{(2\tilde{g}^2 + g^2(1+\chi^2))M_A^2 M_V^2},$$
$$Y = M_W^2 \frac{g'^2(M_A^2 + M_V^2\chi^2)}{(2\tilde{g}^2 + g'^2(1+\chi^2))M_A^2 M_V^2}, \qquad \hat{U} = 0,$$
$$V = 0,$$
$$X = gg' \frac{M_W^2}{M_A^2 M_V^2} \frac{M_A^2 - M_V^2\chi^2}{\sqrt{(2\tilde{g}^2 + g^2(1+\chi^2))(2\tilde{g}^2 + g'^2(1+\chi^2))}}. \tag{19}$$

It is important to notice that these are the electroweak parameters from the pure technicolor sector only. Important negative contributions to $\hat{S}$ (or S) and positive contributions to $\hat{T}$ (or T) can arise from a mass splitting between the techniup and the technidown fermions (which can arise from the ETC sector) or from new nondegenerate lepton doublets, with either Majorana or Dirac neutrinos. A new lepton doublet is actually required in MWT, where it is introduced to cure the SU(2) Witten anomaly, and suffices to bring S and T to within 1σ of the experimental expectation value [13]. Without these extra contributions, if the underlying gauge theory is NMWT (with three colors in the two-index symmetric representation), the naive one-loop contribution to S is $S = 1/\pi \simeq 0.3$. Taking this as the true value of S, the prediction for $\hat{S}$ is almost everywhere in the parameter space within 2σ for a light Higgs and 3σ for a heavy Higgs. If NMWT is very close to the conformal window S can even be smaller: this scenario was considered in Ref. [14], where $\hat{S}$ was taken as a viable input (within 1σ), and the other electroweak parameters, like Y and W, were shown to impose lower bounds on M_A and $\tilde{g}$.

C. Parameter space of NMWT

In our analysis we will take zero κ, since it affects the tree-level anomalous couplings highly constrained by experiments. We take $S = 0.3$ corresponding to its naive value in NMWT.

The remaining parameters are M_A, $\tilde{g}$, s and M_H, with s and M_H having a sizable effect in processes involving the composite Higgs [33].

CDF imposes lower bounds on M_A and $\tilde{g}$ from direct searches of R_1^0 in the $p\bar{p} \to e^+e^-$ process, as shown by the uniformly shaded region in the lower left of Fig. 2. To present this bound we have applied the CDF public results of Ref. [34] to our model. Additional lower bounds on M_A and $\tilde{g}$ come from the electroweak parameters W and Y, as explained in Ref. [14]. The measurements of W and Y exclude the striped region on the lower left in Fig. 2 at 95% confidence level (which corresponds roughly to the 2σ limit of a one-dimensional distribution).

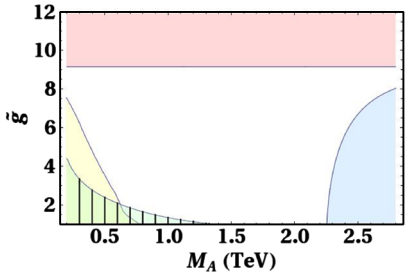

FIG. 2 (color online). Bounds, for $S = 0.3$, in the $(M_A, \tilde{g})$ plane from: (i) CDF direct searches of R_1^0 at the Tevatron, in $p\bar{p} \to e^+e^-$, for $s = 1$ and $M_H = 200$ GeV. The forbidden region is the uniformly shaded one in the left corner. The parameters M_H and s affect indirectly the Tevatron bounds by changing the BR of the Z boson decay to two composite Higgsses. However, we have checked that the effects on the constraints coming from varying the parameter s and M_H are small. (ii) Measurement of the electroweak parameters W and Y at 95% confidence level. The forbidden region is the striped one in the left corner. (iii) The constraint $a > 0$, where a is defined in Eq. (18). The corresponding limiting curve is given by Eq. (21). The forbidden region is the shaded one in the right corner. (iv) Consistency of the theory: no imaginary numbers for physical quantities like F_V and F_A. The forbidden region is the horizontal stripe in the upper part of the figure. The limiting curve here is given by Eq. (20). We repeat that the shaded regions are excluded.

The upper bound for $\tilde{g}$,

$$\tilde{g} < \sqrt{\frac{8\pi}{S}}, \tag{20}$$

is dictated by the internal consistency of the model. For $S = 0.3$ this gives $\tilde{g} \lesssim 9.15$, and is shown by the upper horizontal line in Fig. 2. The upper bound for M_A corresponds to the value for which both WSR's are satisfied in a running regime, and above which a in Eq. (18) becomes negative:

$$M_A^2 < \frac{4\pi F_\pi^2}{S}\left(1 + \frac{1}{\sqrt{1 - \frac{\tilde{g}^2 S}{8\pi}}}\right). \tag{21}$$

This is shown by the lower right curve in Fig. 2.

III. PHENOMENOLOGY

To perform the signal and background analysis we use the CalcHEP package [35] which is a convenient and

powerful tool to investigate the collider phenomenology. The LanHEP package [36] has been used to derive the Feynman rules for the model.

We tested the CalcHEP model implementation in different ways. We have implemented the model in both unitary and t'Hooft-Feynman gauge, and checked the gauge invariance of the physical output. We investigated the custodial technicolor (CT) limit [14] of the model, corresponding to $r_2 = r_3 = 0$, for which $S = 0$ and $M_A = M_V$. If we further require $s = 0$ this model is then identical to the degenerate BESS model (D-BESS) [28] for which results are available in the literature [37]. We find agreement with the latter for the widths and BR's.

New physics signals are expected from the vector meson and the composite Higgs sectors. Here we focus on the production at LHC of the vector mesons through DY and VBF channels, as well as the production of the composite Higgs in association with a weak gauge boson. We compare our results with the ones for Higgsless models [38,39] and on the associate Higgs production with the analysis done by Zerwekh [40].

The signal and background analysis in our study has been performed at the generator level taking into account detector acceptance as discussed below. We believe that a full detector simulation including the true detector geometry, trigger effects, energy smearing, etc. will not change our conclusions on the LHC reach of the technicolor parameter space under study. This is because we have chosen clean leptonic signatures. As a cross check, we have verified that even for the single lepton signature ($\ell + \not{E}_T$)—arising from DY charged vector meson production—our signal and background estimates are in a good agreement with analogous studies by the CMS and ATLAS Collaborations on W' boson production at full detector simulation level (see Sec. 14.4 of Volume II of CMS Technical Design Report [41] and Sec. 21.6.1 of ATLAS Technical Design Report [42]).

A. Heavy vectors: masses, decay widths, and branching ratios

One important consequence of the failure of the second WSR [13,22] is the possible mass spectrum inversion of the vector and axial spin one mesons. In Fig. 3 (left) we plot $M_V - M_A$ as a function of M_A for two reference values of $\tilde{g}$ and $S = 0.3$. For generic values of S the inversion occurs for

$$M^{\rm inv} = \sqrt{\frac{4\pi}{S}} F_\pi. \tag{22}$$

This gives $M^{\rm inv} \simeq 1.6$ TeV for $S = 0.3$, as clearly shown in the plot. Figure 3 (right) shows $M_{R_2^\pm} - M_{R_1^\pm}$ as a function of $M_{R_1^\pm}$, where $R_1^{\pm,0}$ ($R_2^{\pm,0}$) are the lighter (heavier) vector resonances, with tree-level electroweak corrections included. This mass difference is always positive by definition, and the mass inversion becomes a kink in the plot. Away from $M^{\rm inv}$ R_1 (R_2) is an axial (vector) meson for $M_A < M^{\rm inv}$, and a vector (axial) meson for $M_A > M^{\rm inv}$. The mass difference in Fig. 3 is proportional to $\tilde{g}^2$, and becomes relatively small for $\tilde{g} = 2$. The effects of the electroweak corrections are larger for small $\tilde{g}$ couplings. For example, the minimum of $M_{R_2^\pm} - M_{R_1^\pm}$ is shifted from $M^{\rm inv} \simeq 1.59$ TeV to about 1 TeV for $\tilde{g} = 2$. To help the reader we plot in Fig. 4 the actual spectrum for the vector boson masses versus M_A. Preliminary studies on the lattice of MWT and the mass inversion issue appeared in Ref. [18].

The widths of the heavy vectors are displayed in Fig. 5. The lighter meson, R_1, is very narrow. The heavier meson, R_2, is very narrow for small values of $\tilde{g}$. In fact in this case $M_{R_2} \simeq M_{R_1}$, forbidding decays of R_2 to R_1 (+ anything). For large $\tilde{g}$, R_2 is very narrow for large masses, but then becomes broader when the $R_2 \to R_1$, X channels open up, where X is a SM gauge boson. It becomes very broad when the $R_2 \to 2R_1$ decay channel opens up. The former are only important below the inversion point, where R_1 is not too heavy. The latter is only possible when R_2 is essentially a spin one vector and $M_{R_2} > 2M_{R_1}$.

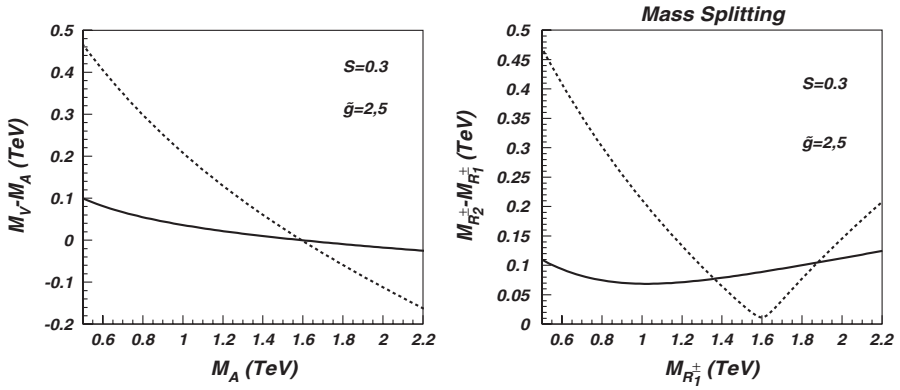

FIG. 3. Mass splittings $M_V - M_A$ (left) and $M_{R_2^\pm} - M_{R_1^\pm}$ (right). The dotted lines are for $\tilde{g} = 5$ while the solid lines are for $\tilde{g} = 2$.

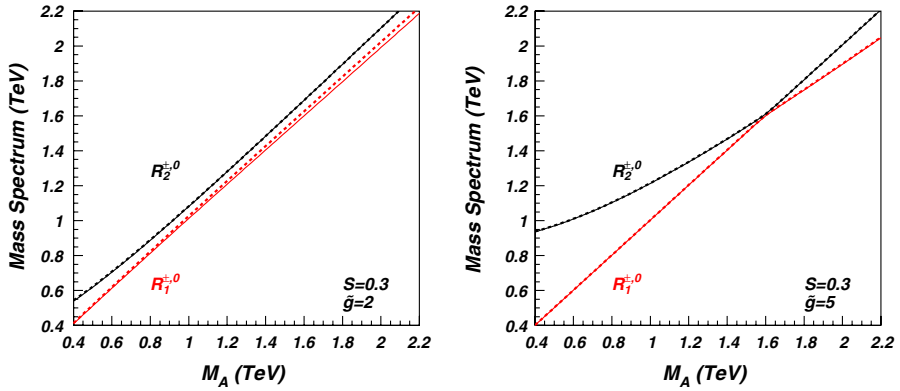

FIG. 4 (color online). The mass spectrum of the $M_{R_{1,2}^{\pm,0}}$ vector mesons versus M_A for $\tilde{g} = 2$ (left) and $\tilde{g} = 5$ (right). The masses of the charged vector mesons are denoted by solid lines, while the masses of the neutral mesons are denoted by dashed lines.

The narrowness of R_1 (and R_2, when the $R_2 \to R_1$, X channels are forbidden) is essentially due to the small value of the S parameter. In fact for $S = 0$ the trilinear couplings of the vector mesons to two scalar fields of the strongly interacting sector vanish. This can be understood as follows: the trilinear couplings with a vector resonance contain a derivative of either the Higgs or the technipion, and this can only come from r_3 in Eq. (1). Since $r_3 = 0$ implies $S = 0$, as Eqs. (15) and (16) show explicitly, it follows that the decay width of R_1 and R_2 to two scalar fields vanishes as $S \to 0$. As a consequence, for $S = 0$ the vector meson decays to the longitudinal SM bosons are highly suppressed, because the latter are nothing but the eaten technipions. (The couplings to the SM bosons do not vanish exactly because of the mixing with the spin one resonances.) A known scenario in which the widths of R_1 and R_2 are highly suppressed is provided by the D-BESS model [37], where the spin one and the spin zero resonances do not interact. Therefore, in D-BESS *all* couplings involving one or more vector resonances and one or more scalar fields vanish, not just the trilinear coupling with one vector field. The former scenario requires $r_2 = r_3 = s = 0$, the latter only requires $r_3 = 0$. A somewhat intermediate scenario is provided by CT, in which $r_2 = r_3 = 0$ but $s \neq 0$. Narrow spin one resonances seem to be a common feature in various models of dynamical electroweak symmetry

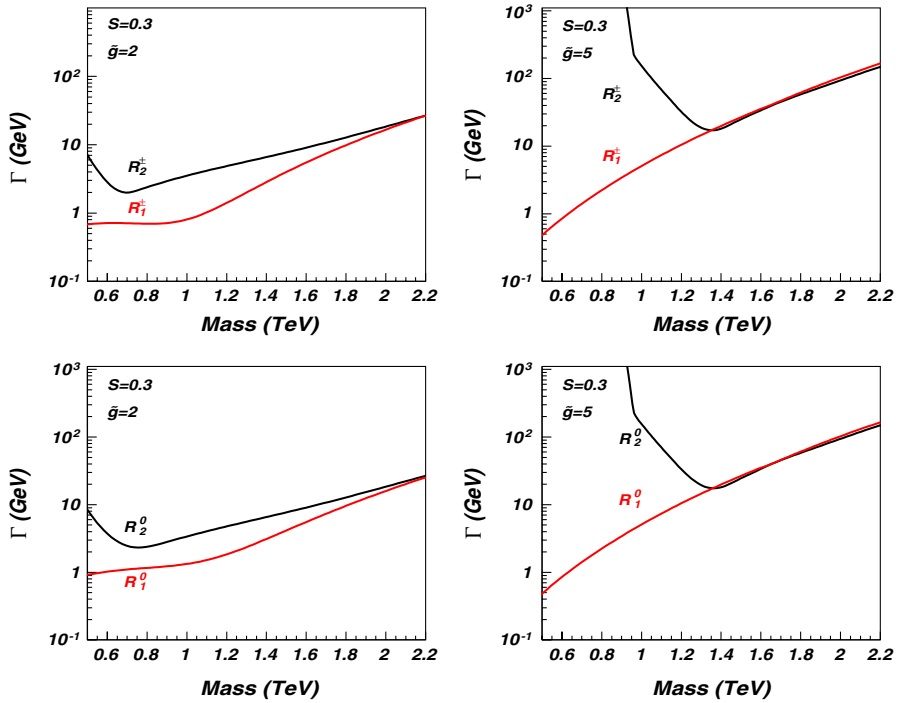

FIG. 5 (color online). Decay width of the charged (first row) and neutral (second row) vector mesons for $S = 0.3$ and $\tilde{g} = 2, 5$. We take $M_H = 0.2$ TeV, $s = 0$.

breaking. (see, for example, Ref. [43]). Within our effective Lagrangian (1) this property is linked to having a small S parameter. If it turns out that broader spin one resonances are observed at the LHC this fact can be accounted for by including operators of mass dimension greater than four, as shown in Sec. III E.

The R_1 branching ratios are shown in Fig. 6. The wild variations observed in the plots around 1.6 TeV reflect the mass inversion discussed earlier. Here the mixing between R_1^a and $\tilde{W}^a$, with $a = 0, \pm$, vanishes, suppressing the decay to SM fermions.

The other observed structure for the decays in ZH and WH, at low masses, is due to the opposite and competing contribution coming from the technicolor and electroweak sectors. This is technically possible since the coupling of the massive vectors to the longitudinal component of the gauge bosons and the composite Higgs is suppressed by the small value of S.

Now we consider the R_2 BR's displayed in Fig. 7. With R_2 being heavier than R_1 by definition, new channels like $R_2 \to 2R_1$ and $R_2 \to R_1 X$ show up, where X denotes a SM boson. Notice that there is a qualitative difference in the R_2 decay modes for small and large values of $\tilde{g}$. First, for small $\tilde{g}$ the $R_2 - R_1$ mass splitting is not large enough to allow the decays $R_2 \to 2R_1$ and $R_2 \to R_1 H$, which are instead present for large $\tilde{g}$. Second, for small $\tilde{g}$ there is a wide range of masses for which the decays to R_1 and a SM vector boson are not possible, because of the small mass splitting. The BR's to fermions do not drop at the inversion point, because the $R_2 - \tilde{W}$ mixing does not vanish.

B. Drell-Yan production: $p, p \to R_{1,2}$

Spin one resonances can be produced at the LHC through the DY processes $pp \to R_{1,2}$. The corresponding cross sections are shown in Fig. 8. Consider first the

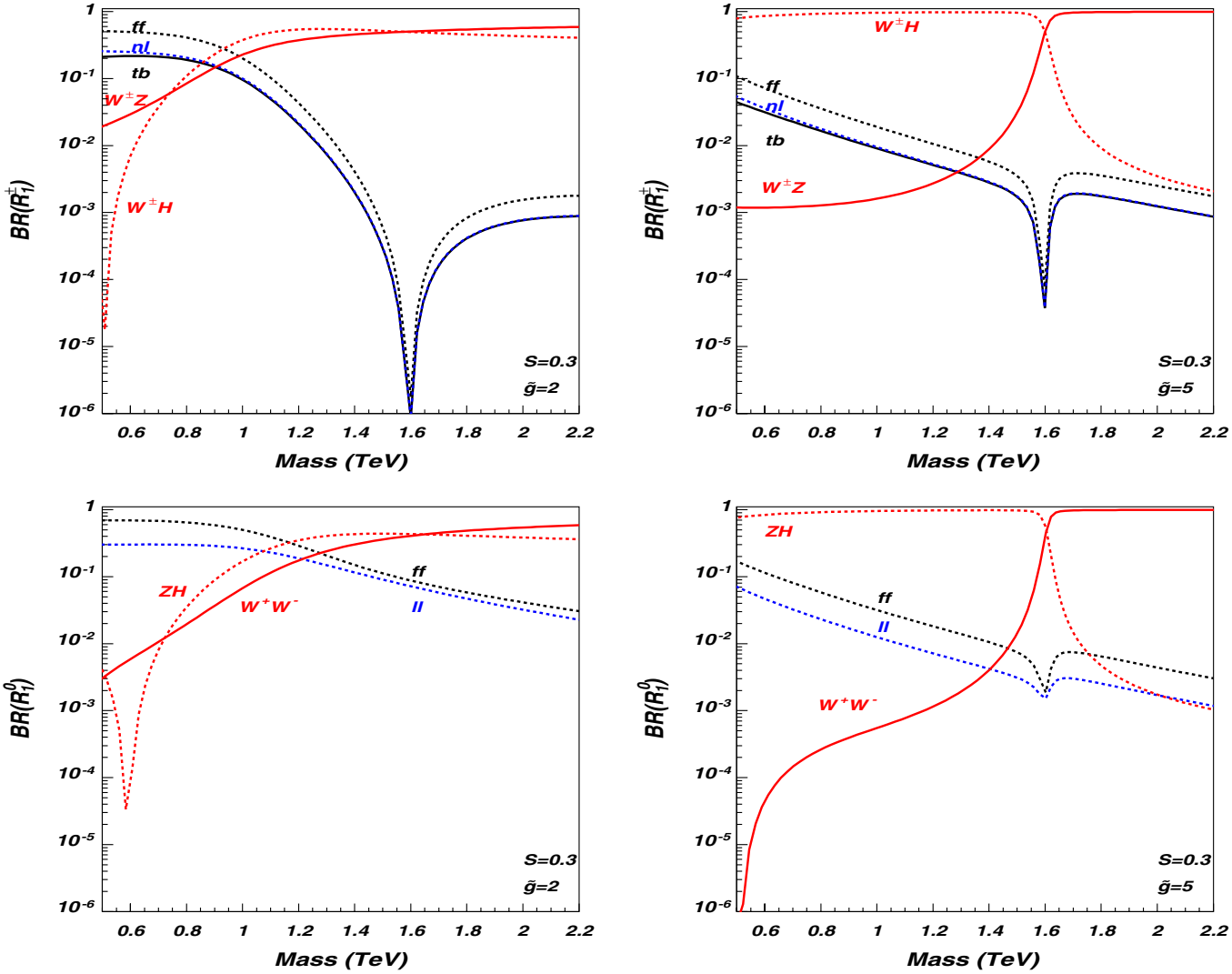

FIG. 6 (color online). Branching ratios of the charged (first row) and neutral (second row) R_1 resonance for $S = 0.3$ and $\tilde{g} = 2, 5$. We take $M_H = 0.2$ TeV, $s = 0$.

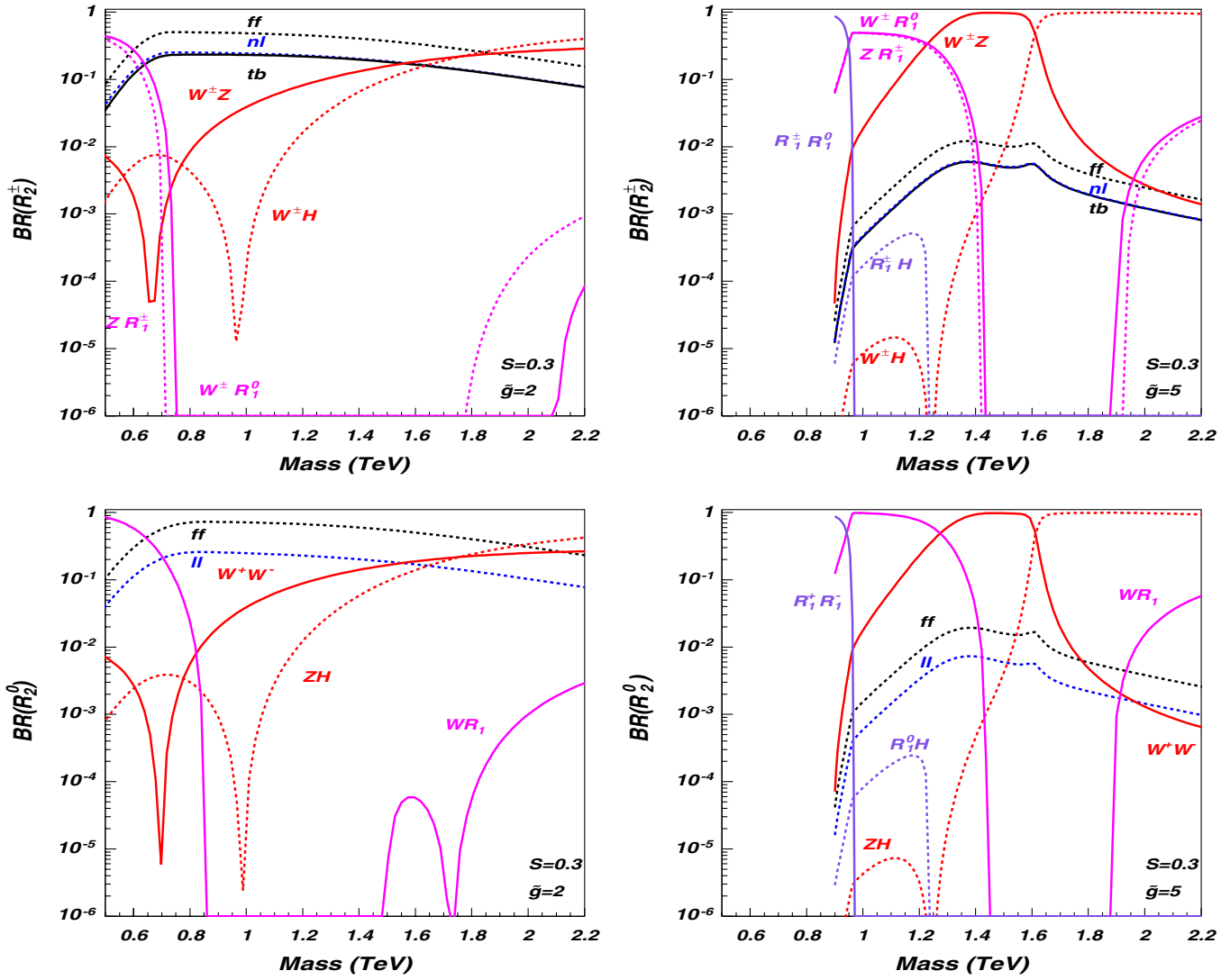

FIG. 7 (color online). Branching ratios of the charged (first row) and neutral (second row) R_2 resonance for $S = 0.3$ and $\tilde{g} = 2, 5$. We take $M_H = 0.2$ TeV, $s = 0$.

production of $R_2^{\pm}$, since the latter is less affected than $R_1^{\pm}$ by the presence of the mass inversion point. The cross section decreases as $\tilde{g}$ grows, because of the reduced $R_2 - \tilde{W}$ mixing. In going from $\tilde{g} = 2$ to $\tilde{g} = 5$ the decrease in the production cross section of $R_2^{\pm}$ is roughly 1 or 2 orders of magnitude. This is expected since the leading-order contribution to the coupling between $R_2^{\pm}$ and the fermions is explicitly proportional to $\tilde{g}^{-2}$, as it is in the D-BESS model [37].

As explained in Sec. III A the $R_1^{\pm}$ resonance becomes fermiophobic at the inversion point, causing the corresponding DY production to drop. In our model the new vectors are fermiophobic only at the mass inversion point differentiating it from a class of Higgsless model in which the charged W' resonance is taken to have strongly suppressed couplings to the light fermions for any value of the vector masses.

To estimate the LHC reach for DY production of the $R_{1,2}^0$ and $R_{1,2}^{\pm}$ resonances we study the following lepton signatures:

(1) $\ell^+\ell^-$ signature from the process $pp \to R_{1,2}^0 \to \ell^+\ell^-$
(2) $\ell + \not{E}_T$ signature from the process $pp \to R_{1,2}^{\pm} \to \ell^{\pm}\nu$
(3) $3\ell + \not{E}_T$ signature from the process $pp \to R_{1,2}^{\pm} \to ZW^{\pm} \to 3\ell\nu$,

where ℓ denotes a charged lepton—electron or muon and $\not{E}_T$ is the missing transverse energy. We apply detector acceptance cuts of $|\eta^{\ell}| < 2.5$ and $p_T^{\ell} > 15$ GeV on the rapidity and transverse momentum of the leptons.

For all three signatures we have evaluated only irreducible electroweak SM backgrounds leading to the same final state. These backgrounds are the dominant ones for the signatures under study. For example, the potentially large reducible $t\bar{t}$ background for signature (2) is several times less than the $pp \to \ell\nu$ background which we took into

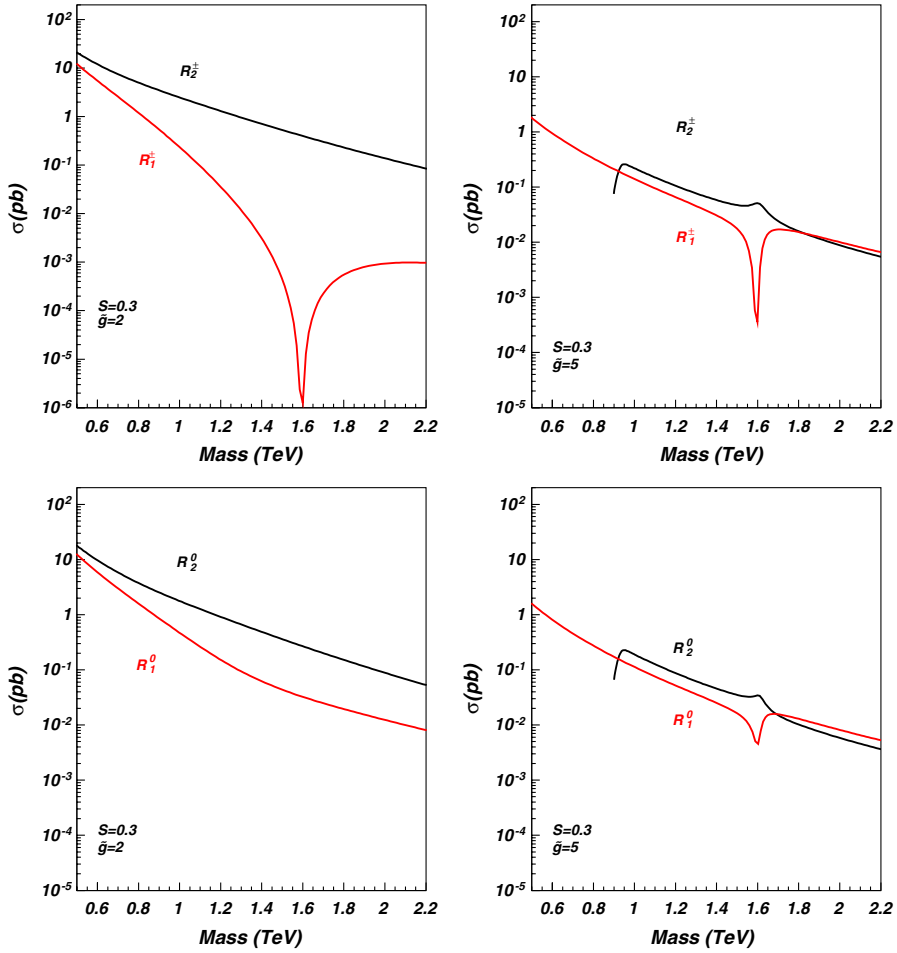

FIG. 8 (color online). Drell-Yan production of the $R^{\pm}_{1,2}$ (first row) and $R^{0}_{1,2}$ (second row) resonances, with $S = 0.3$ and $\tilde{g} = 2, 5$.

account. For signature (3) we have evaluated only the irreducible $pp \to 3\ell\nu$ SM background. The second-most important background for signature (3) comes from the process $pp \to ZZ$ when one of the leptons escapes detection. For simplicity we have neglected this background which is at least a factor of 3 smaller than the leading one.

Finally there are various sources of systematical uncertainties entering the signal and background determination. These uncertainties lead to a reduction of the signal sensitivity and have been estimated by the LHC collaborations. It has been shown [41,42] that taking uncertainties in the determination of the parton density function (PDF), the

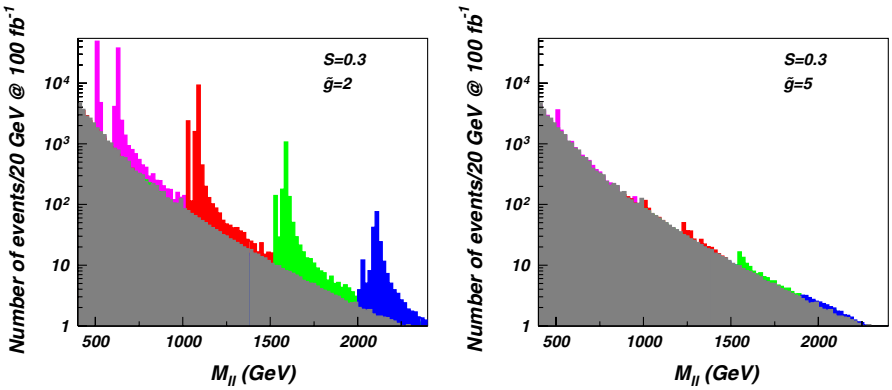

FIG. 9 (color online). Dilepton invariant mass distribution $M_{\ell\ell}$ for $pp \to R^{0}_{1,2} \to \ell^{+}\ell^{-}$ signal and background processes. We consider $\tilde{g} = 2, 5$, respectively, and masses $M_A = 0.5$ TeV (purple), $M_A = 1$ TeV (red), $M_A = 1.5$ TeV (green) and $M_A = 2$ TeV (blue).

missing transverse energy, the QCD scale and systematic detector uncertainties into account leads to a decrease in signal sensitivity (significance) by 10–15% for DY processes. However it was also shown that taking into account corrections at next-to leading order by introducing a K-factor 1.35 for the signal and background leads to an increase in signal sensitivity of 6%. Such a range of variation in sensitivity does not qualitatively affect any conclusions regarding the LHC reach in our paper.

For signature (1) we use the dilepton invariant mass distribution $M_{\ell\ell}$ to separate the signal from the background. For signatures (2) and (3) we use instead the transverse mass variables M_ℓ^T and $M_{3\ell}^T$ [44]:

$$(M_\ell^T)^2 = [\sqrt{M^2(\ell) + p_T^2(\ell)} + |\not{p}_T|]^2 - |\vec{p}_T(\ell) + \vec{\not{p}}_T|^2 \tag{23}$$

$$(M_{3\ell}^T)^2 = [\sqrt{M^2(\ell\ell\ell) + p_T^2(\ell\ell\ell)} + |\not{p}_T|]^2 - |\vec{p}_T(\ell\ell\ell) + \vec{\not{p}}_T|^2. \tag{24}$$

We also add a cut on the transverse missing energy $\not{E}_T > 15$ GeV. We consider the representative parameter space points $\tilde{g} = 2, 5$ and $M_A = 0.5, 1, 1.5, 2$ TeV for our plots and discussion.

The invariant mass and transverse mass distributions for signatures (1)–(3) are shown in Figs. 9–11. In the left frames of Figs. 9 and 10, corresponding to $\tilde{g} = 2$, clear signals from the leptonic decays of $R_{1,2}^0$ and $R_{1,2}^\pm$ are seen even for 2 TeV resonances. Moreover Fig. 9 demonstrates that for $\tilde{g} = 2$ both peaks from R_1^0 and R_2^0 may be resolved. For the chosen bin size of 20 GeV the lepton energy resolution effects which are of the order of $0.2\sqrt{E}$ (where E is the lepton energy in GeV) will not visibly affect the presented distributions. In the case of signature (2) a double-resonance peak is also seen at low mass, but the transverse mass distribution M_ℓ^T is not able to resolve the signal pattern as precisely as the $M_{\ell\ell}$ distribution for signature (1), because of the presence of missing transverse momenta from the neutrino. Moreover, the instrumental missing transverse momenta related to the various detector effects can further affect the M_l^T distribution. This point requires investigation using a full detector simulation. Signature (2) has an interesting peculiarity: For larger masses only a single resonance is visible because the R1 coupling to fermions is strongly suppressed. This is a distinguishing footprint of the NMWT model at higher masses closer to the inversion point: only a single peak from the $R_2^\pm$ will appear in the single lepton channel while a double peak should be visible in the dilepton channel.

Let us now turn to the case of $\tilde{g} = 5$ in the right frames of Figs. 9 and 10. For large $\tilde{g}$ the Rff couplings are suppressed, so observing signatures (1) and (2) could be problematic (quantitative results for the LHC reach for all signatures are presented below). However, for large $\tilde{g}$, the triple-vector coupling is enhanced, so one can observe a clear signal in the $M_{3\ell}^T$ distribution presented in Fig. 11. At low masses the decays of the heavy vector mesons to SM gauge bosons are suppressed and the signal disappears. This mass range can, however, be covered with signatures (1) and (2). Furthermore the associate Higgs production can also access this mass range as seen from the analysis of the WZZ and ZZZ invariant mass distributions in Sec. III D.

We end this section by quantifying the LHC reach for signatures (1)–(3) in terms of the luminosity required to observe the $R_{1,2}$ mass peaks at a significance of 3 and 5 sigma. To do so we define the signal as the difference between the NMWT cross section and the SM cross section in a certain mass window around the peak. We optimize the invariant or transverse mass window cuts, on a case by case basis, for each signature and parameter space point. For example, signatures (2) and (3) require asymmetric mass window cuts since the transverse one- and tri-lepton mass distribution have low-end tails. We single out the most significant peak when applying the mass window cut. The significance of the signal is then defined as the number of signal events divided by the square root of the number of background events when the number of events is large,

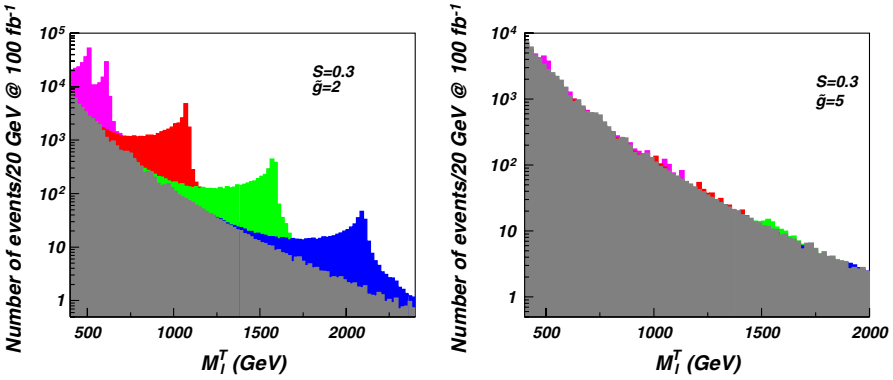

FIG. 10 (color online). M_ℓ^T mass distribution for $pp \to R_{1,2}^\pm \to \ell^\pm \nu$ signal and background processes. We consider $\tilde{g} = 2$, 5, respectively, and masses $M_A = 0.5$ TeV (purple), $M_A = 1$ TeV (red), $M_A = 1.5$ TeV (green) and $M_A = 2$ TeV (blue).

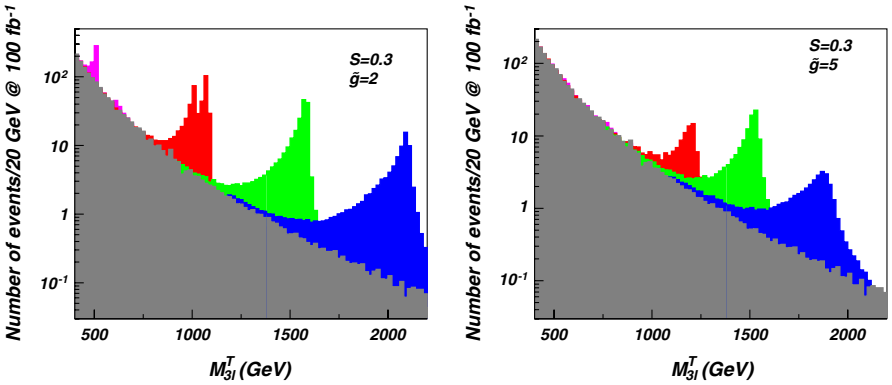

FIG. 11 (color online). $M^T_{3\ell}$ mass distribution for $pp \to R^{\pm}_{1,2} \to ZW^{\pm} \to 3\ell\nu$ signal and background processes. We consider $\tilde{g} = 2$, 5, respectively, and masses $M_A = 0.5$ TeV (purple), $M_A = 1$ TeV (red), $M_A = 1.5$ TeV (green) and $M_A = 2$ TeV (blue).

while a Poisson distribution is used when the number of events is small.

The luminosity required for 5σ and 3σ significance for signature (1) is shown in the first row of plots in Fig. 12 as a function of the mass of the resonance while the signal and background cross sections are shown in the second row of plots. For $\tilde{g} = 2$ one can see that even for 5 fb^{-1} of integrated luminosity the LHC will observe vector mesons up to 2 TeV mass through signature (1). On the other hand, for $\tilde{g} = 5$ even with 100 fb^{-1} integrated luminosity one

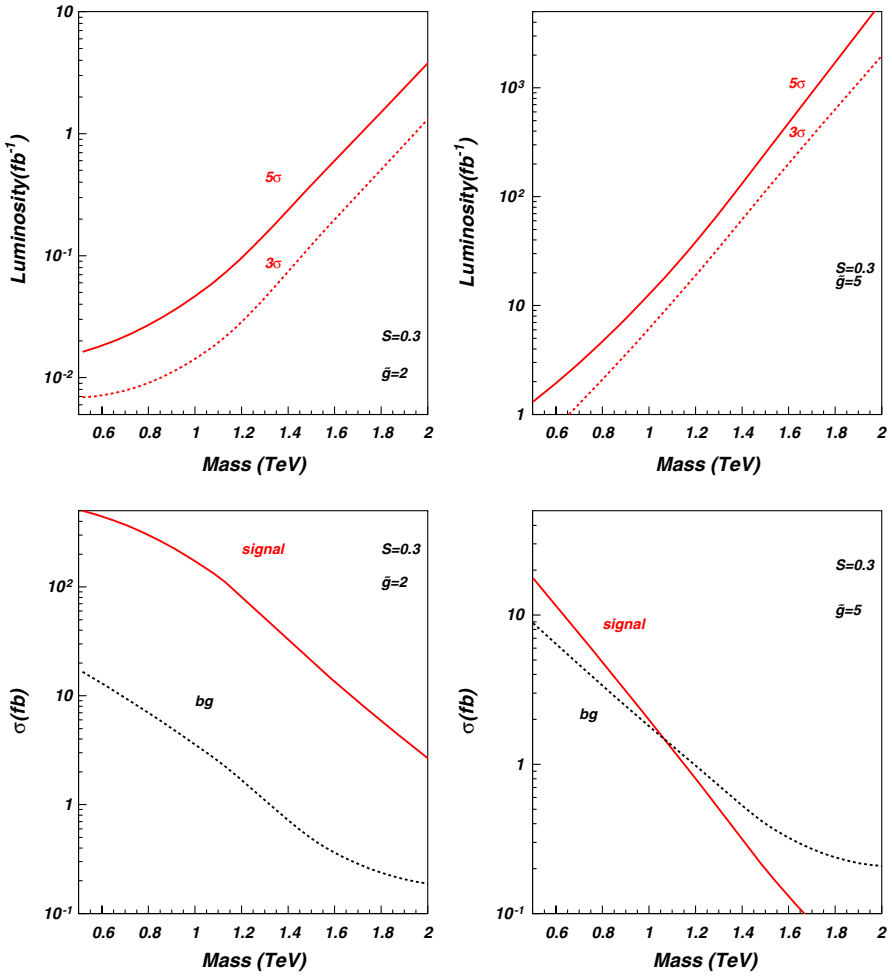

FIG. 12 (color online). LHC reach for the $R^0_{1,2}$ resonance signal in $pp \to R^0_{1,2} \to e^+e^-$ with $S = 0.3$ and $\tilde{g} = 2$, 5. Top row: the required integrated luminosity for achieving a 5σ and a 3σ significance. Bottom row: the signal and background cross sections for this process.

would not be able to observe vector mesons heavier than 1.4 TeV in this channel. The reach of the LHC for signature (2) is quite similar to the one for signature (1) for $\tilde{g} = 2$ but less promising for $\tilde{g} = 5$ as one can see in Fig. 13.

The LHC reach for signature (3) is presented in Fig. 14. For $\tilde{g} = 2$ the LHC will cover the whole mass range under study with 10 fb^{-1} of integrated luminosity through signature (3). For $\tilde{g} = 5$ it will be able to cover the large mass region inaccessible to signatures (1) and (2) through signature (3) with an integrated luminosity of 10–50 fb^{-1} while the low-mass region could be covered by signatures (1) and (2) with an integrated luminosity of 10–100 fb^{-1}. Thus signature (3) is, in a very important way, complementary to signatures (1) and (2).

C. Vector boson fusion production: $p, p \to R_{1,2}, j, j$

VBF is potentially an important channel for vector meson production, especially in theories in which the vector resonances are quasi-fermiophobic.

We consider VBF production of the charged R_1 and R_2 vectors. We impose the following kinematical cuts on the jet transverse momentum p_T^j, energy E^j, and rapidity gap $\Delta\eta^{jj}$, as well as rapidity acceptance $|\eta^j|$ [38,39]:

$$|\eta^j| < 4.5, \qquad p_T^j > 30 \text{ GeV}, \qquad E^j > 300 \text{ GeV}, \qquad \Delta\eta^{jj} > 4. \tag{25}$$

The VBF production cross section for the charged R_1 and R_2 vector resonances is shown in Fig. 15 for the set of cuts given by Eq. (25). An interesting feature of the VBF production is the observed crossover around the mass degeneracy point for $\tilde{g} = 5$. This is a direct consequence of the fact that the $R_{1,2}$ resonances switch their vector/axial nature at the inversion point. For small $\tilde{g}$ the crossover does not occur due to the interplay between the electroweak and the technicolor corrections. In D-BESS VBF processes are not very relevant, since there are no direct interactions between the heavy mesons and the SM vectors. However in fermiophobic Higgsless models VBF is the main pro-

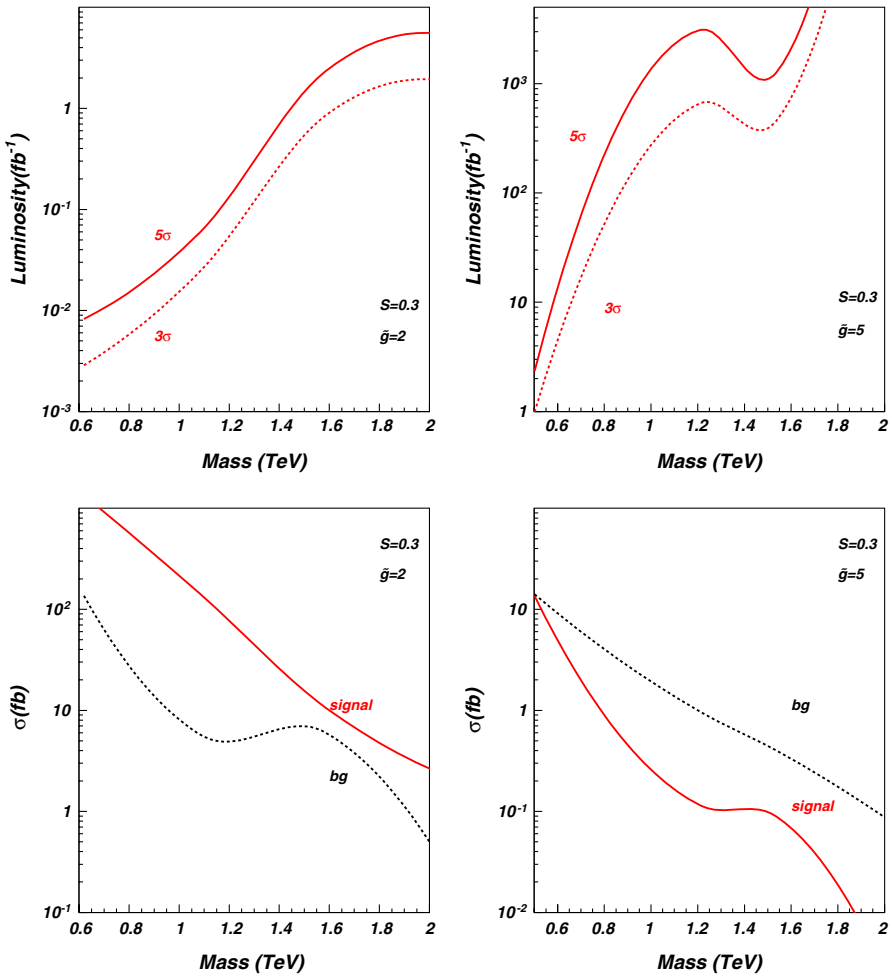

FIG. 13 (color online). LHC reach for the $R_{1,2}^{\pm}$ resonance signal in $pp \to R_{1,2}^{\pm} \to \ell \not{E}_T$ signature with $S = 0.3$ and $\tilde{g} = 2, 5$. Top row: the required integrated luminosity for achieving a 5σ and a 3σ significance. Bottom row: the signal and background cross sections for this process.

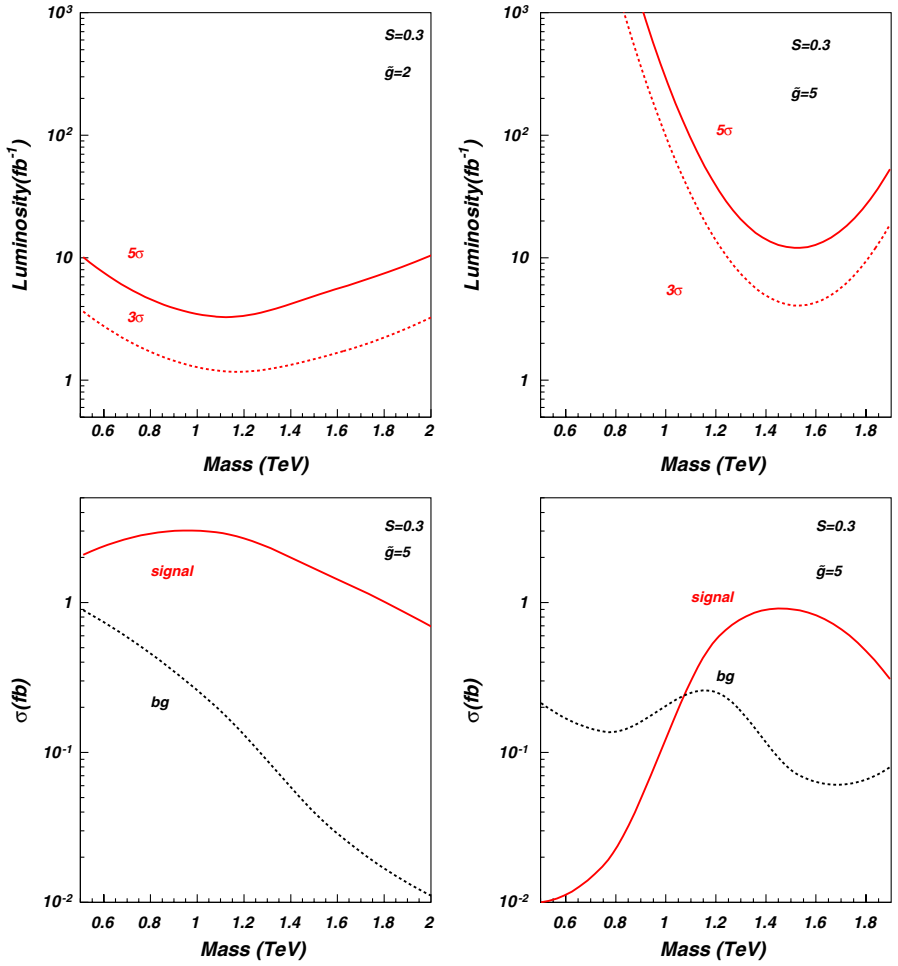

FIG. 14 (color online). LHC reach for the $R^{\pm}_{1,2}$ resonance signal in $pp \to R^{\pm}_{1,2} \to W^{\pm}Z \to 3\ell \not{E}_T$ signature with $S = 0.3$ and $\tilde{g} = 2, 5$. Top row: the required integrated luminosity for achieving a 5σ and a 3σ significance. Bottom row: the signal and background cross sections for this process.

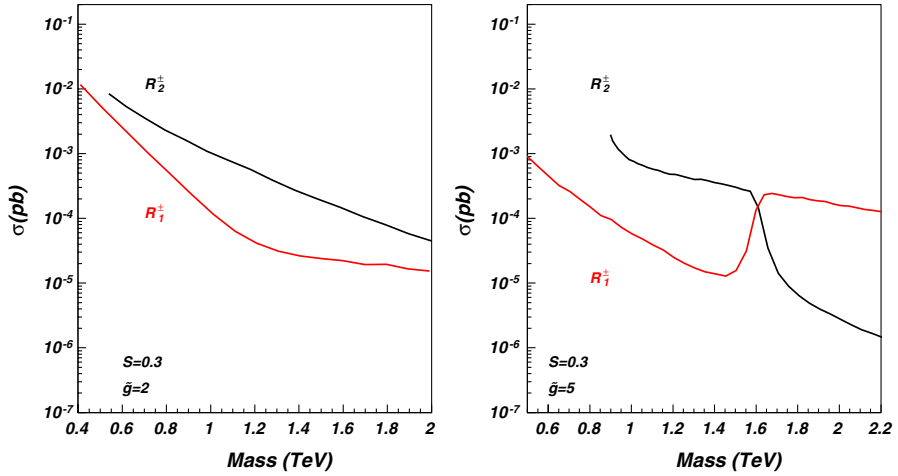

FIG. 15 (color online). Vector boson fusion production cross sections for the $R^{\pm}_{1,2}$ resonances, with $S = 0.3$ and $\tilde{g} = 2, 5$. The jet cuts are $|\eta^j| < 4.5$, $p_T^j > 30$ GeV, $E^j > 300$ GeV, $\Delta\eta^{jj} > 4$. See text for details.

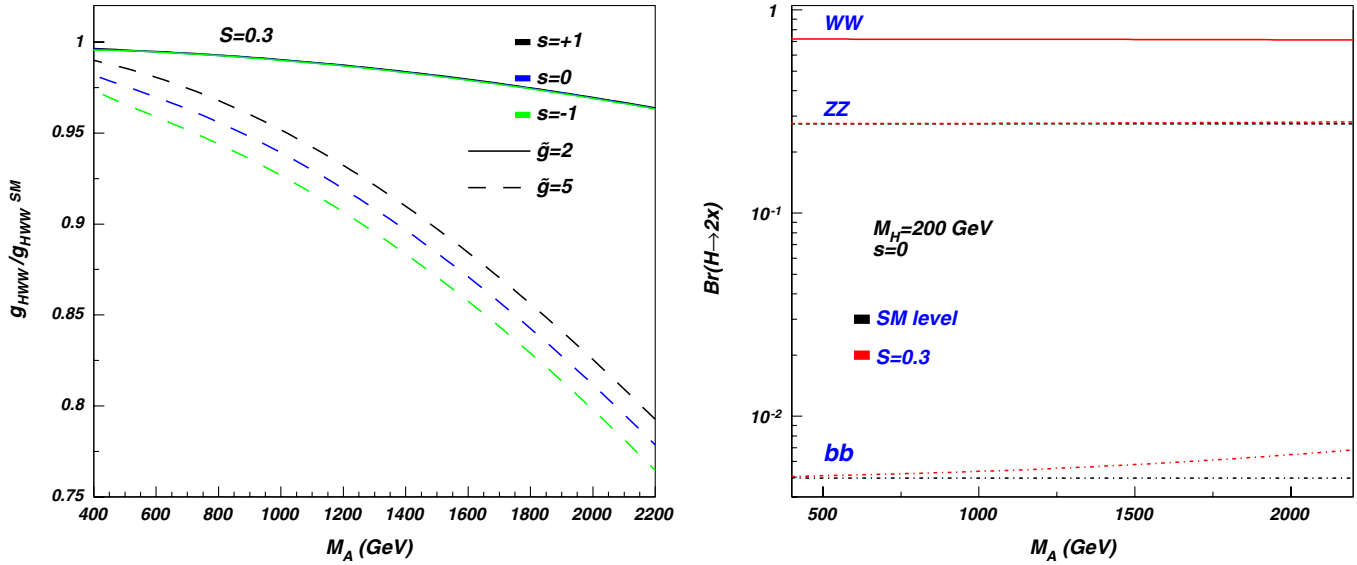

FIG. 16 (color online). Left: $g_{HWW}/g_{HWW}^{\mathrm{SM}}$ ratio as a function of M_A. The behavior of the g_{HZZ} coupling is identical to the g_{HWW} one. Results are presented for $S = 0.3$, $\tilde{g} = 2$ and 5 (solid and dashed lines, respectively), and for $s = (+1, 0, -1)$ (black, blue and green colors, respectively). Right: branching ratios of the composite Higgs (red) and SM Higgs (black) as function M_A with $s = 0$. $M_H = 200$ GeV.

duction channel of the heavy resonances. Since the production rate of $R^{\pm}_{1,2}$ is below 1 fb VBF is not a promising channel at the LHC.

D. Composite Higgs phenomenology

The composite Higgs phenomenology is interesting due to its interactions with the new massive vector bosons and their mixing with SM gauge bosons. We first analyze the Higgs coupling to the W- and Z- gauge bosons. In Fig. 16 (left) we present the g_{HWW}/g_{HWW}^{SM} ratio as a function of M_A. The behavior of the g_{HZZ} and g_{HWW} couplings is identical. We keep fixed $S = 0.3$ and consider two values of $\tilde{g}$, 2 (solid line) and 5 (dashed line). We repeat the plots for three choices of the s parameter $(+1, 0, -1)$ depicted in black, blue and green colors, respectively. The deviation of g_{HWW} from g_{HWW}^{SM} increases with M_A due to the fact that we hold the S parameter fixed. One reaches deviations from the SM couplings of 20% when $M_A \simeq 2$ TeV. This is reflected in the small deviations of the Higgs branching ratios when compared with the SM ones as shown in Fig. 16 (right). Here we used as reference point $s = 0$.

The presence of the heavy vectors is prominent in the associate production of the composite Higgs with SM vector bosons, as first pointed out in [40]. Parton level Feynman diagrams for the $pp \to WH$ and $pp \to ZH$ processes are shown in Fig. 17 (left) and Fig. 17 (right), respectively. The resonant production of heavy vectors can enhance HW and ZH production by a factor of 10 as one can see in Fig. 18 (right). This enhancement occurs for low values of the vector meson mass and large values of $\tilde{g}$. This behavior is shown in Fig. 18 (right) for $\tilde{g} = 5$. These are values of the parameters not excluded by Tevatron data (see Fig. 2).

The contribution from the heavy vector to $pp \to VH$ ($V = W^{\pm}, Z$ can be clearly identified from the peaks in the invariant mass distributions of WZZ or ZZZ presented in Fig. 19. One should consider these distributions as qualitative ones, since at the experimental level WZZ or ZZZ invariant masses will be reconstructed from leptons and jets in the final state with appropriate acceptance cuts applied. However, one can eventually expect that visibility of the signal will remain. Taking into account leptonic branching ratios of the two Z-bosons and the hadronic

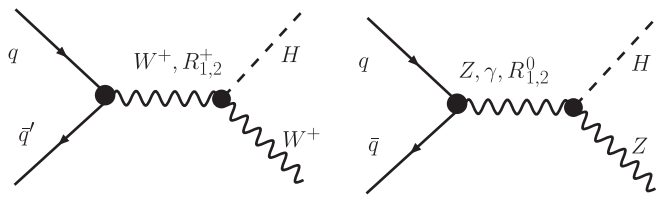

FIG. 17. Feynman diagrams for the composite Higgs production in association with SM gauge bosons.

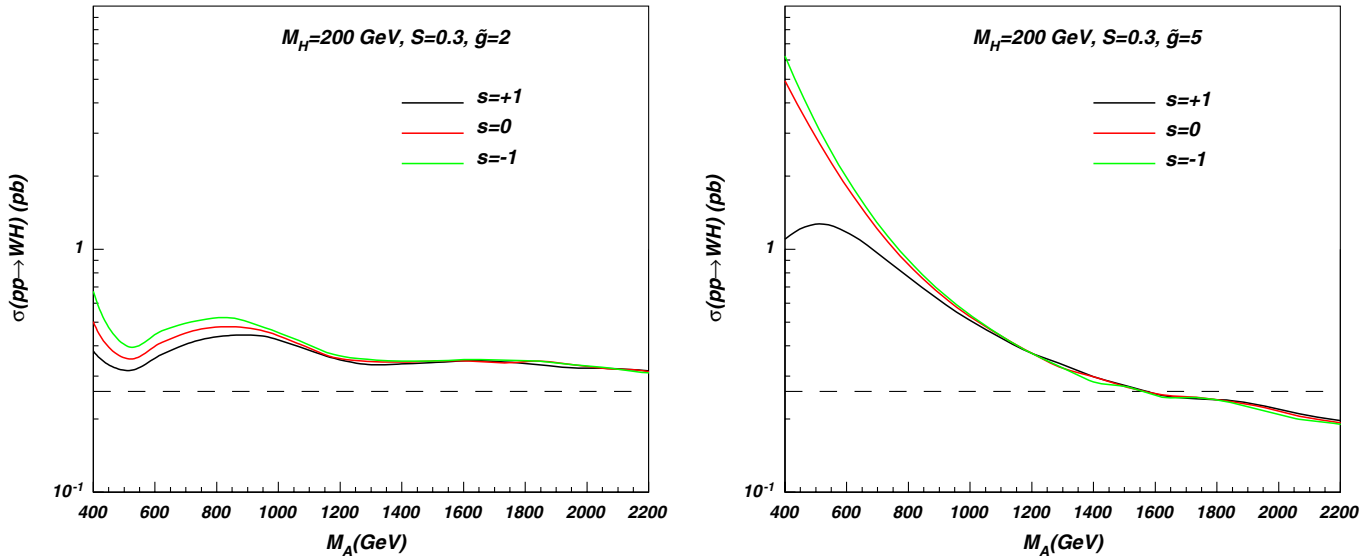

FIG. 18 (color online). The cross section for $pp \to WH$ production (W^+H and W^-H modes are summed up) versus M_A for $S = 0.3$, $s = (+1, 0, 1)$ and $\tilde{g} = 2$ (left) and $\tilde{g} = 5$ (right). The dashed line at the bottom indicates the SM cross-section level.

branching ratios for the third gauge boson (W or Z) we estimate about 40 clean events under the peak with negligible background. The second broader vector peak will not be observed. We have also analyzed the composite Higgs production in vector boson fusion processes $pp \to Hjj$. We find that it is not enhanced with respect to the corresponding process in the SM as it is clear from Fig. 20. The behavior of the $\sigma(pp \to Hjj)$ as function of M_A traces the one of the Higgs-gauge bosons coupling shown in Fig. 16.

E. Extending the parameter space

In Sec. III A we saw that the vector resonances are very narrow. The only exception occurs for the R_2 meson, when the $R_2 \to R_1$, X and $R_2 \to 2R_1$ channels are important (X denotes a SM gauge boson). The origin of this can be attributed to the fact that in writing Eq. (1) we used only renormalizable operators. Consider, for example, the operator [1,45]

$$-\frac{2\gamma}{v^2}\,\mathrm{Tr}[F_{\mathrm{L}\mu\nu}MF_{\mathrm{R}}^{\mu\nu}M^{\dagger}]. \tag{26}$$

This operator was introduced many years ago by Kaymakcalan and Schechter in [45] and appeared for the first time in DEWSB effective Lagrangians in [1]. The effects of a similar Lagrangian term have been also recently discussed, in the context of a four-site Higgsless model, by Chivukula and Simmons [46]. This term affects

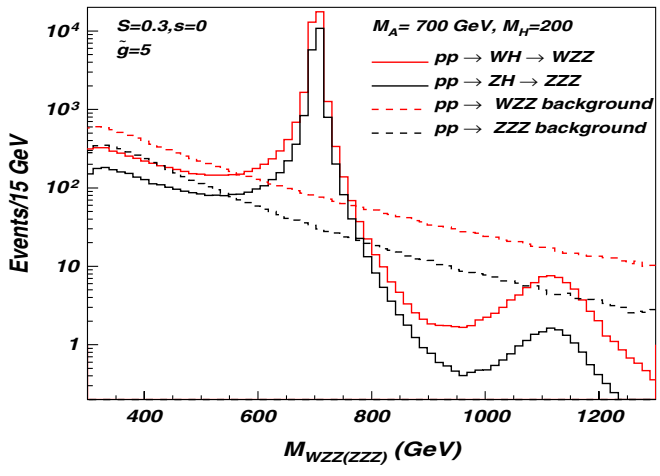

FIG. 19 (color online). Invariant mass distributions of WZZ or ZZZ for signal (solid lines) and background (dashed lines) for 100 fb^{-1}.

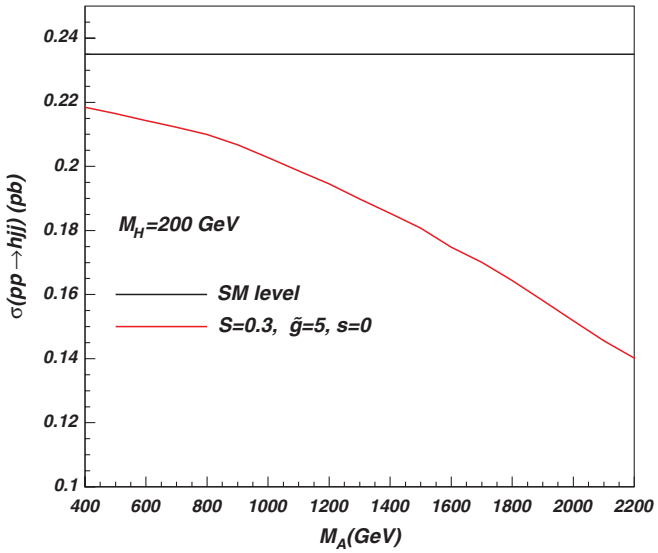

FIG. 20 (color online). Composite Higgs production cross section via the VBF mechanism.

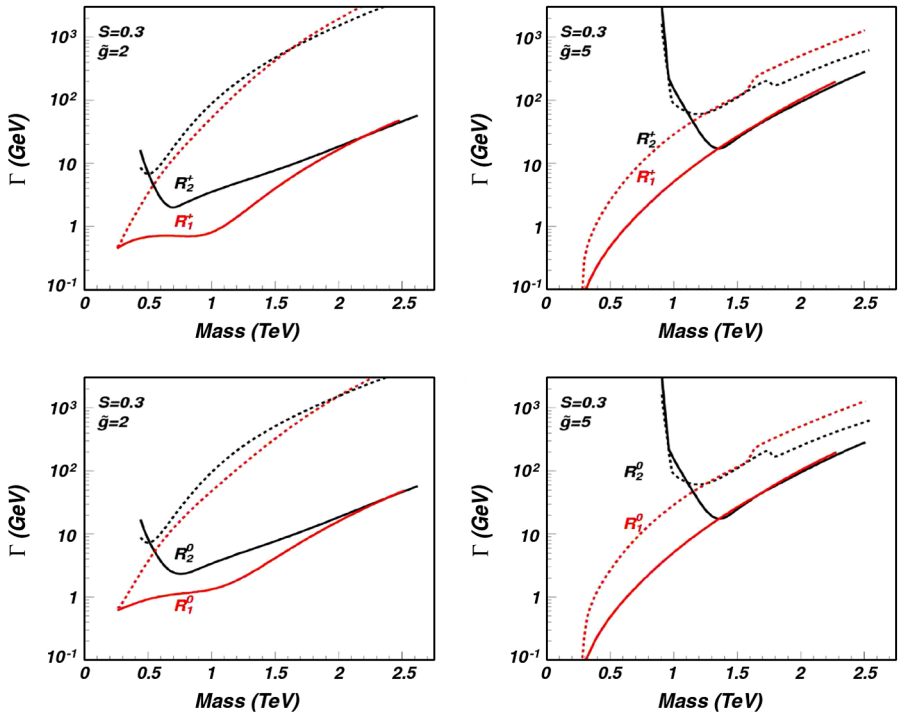

FIG. 21 (color online). Decay width of the charged (first row) and neutral (second row) vector mesons for $S = 0.3$ and $\tilde{g} = 2, 5$. The solid lines correspond to $\gamma = 0$, the dashed lines correspond to $\gamma = -0.5$. We take $M_H = 0.2$ TeV, $s = 0$.

several couplings. For example the $g_{V\pi\pi}$ coupling reads

$$g_{V\pi\pi} = \frac{F_V M_V}{2F_\pi^2}\left[1 - \frac{1+\gamma}{1-\gamma}\frac{F_A^2}{M_A^2}\frac{M_V^2}{F_V^2}\right]. \tag{27}$$

Taking either the $M_A \to \infty$ or the $\gamma \to -1$ limit returns the known formula for $g_{\rho\pi\pi}$ in QCD. To better appreciate the physical content of this term we combine Eqs. (1) and (26) yielding the following kinetic terms for the vector and axial states:

$$-\frac{1+\gamma}{4}(\partial_\mu V_\nu - \partial_\nu V_\mu)^2 - \frac{1-\gamma}{4}(\partial_\mu A_\nu - \partial_\nu A_\mu)^2. \tag{28}$$

From this it follows that requiring the vector mesons to be nontachyonic propagating fields implies $-1 < \gamma < 1$. Moreover it is unreasonable to take γ too close to either -1 or 1, because this would naturally lead to infinitely large masses for the vector mesons.

Taking a value of γ not close to ± 1 but different from zero has a large impact on the meson widths. In Fig. 21 the R_1 and R_2 widths are shown for both $\gamma = 0$ (solid lines) and $\gamma = -0.5$ (dashed lines). The widths can increase by 2 orders of magnitude. The DY production of the heavy vectors is unaffected by γ, at the tree-level, since the fermion couplings to the vector mesons do not depend on it. We have also checked that the contributions from this term do not substantially affect the other results.

IV. CONCLUSIONS

We have analyzed the potential of the Large Hadron Collider to observe signatures of phenomenologically viable walking technicolor models. We studied and compared the Drell-Yan and vctor boson fusion mechanisms for the production of composite heavy vectors. The DY production mechanism constitutes the most promising way to detect and study the technicolor spin one states.

We have compared, when possible, with earlier analysis and shown that our description reproduces all of the earlier results while extending them by incorporating basic properties of walking dynamics such as the mass relation between the vector and axial spin one resonances.

LHC can be sensitive to spin one states as heavy as 2 TeV. One TeV spin one states can be observed already with 100 pb^{-1} integrated luminosity in the dilepton channel. The VBF production of heavy mesons is, however, suppressed and will not be observed. The enhancement of the composite Higgs production is another promising signature.

We identified distinct DY signatures which allow to cover at the LHC, in a complementary way, a great deal of the model's parameter space.

ACKNOWLEDGMENTS

We gladly thank Neil Christensen for providing us an improved CalcHEP batch interface and Elena Vataga for discussions related to the experimental signatures. We thank Dennis D. Dietrich for discussions. The work of R. F., M. T. F., M. J., and F. S. is supported by the Marie Curie Excellence Grant under Contract No. MEXT-CT-2004-013510. The work of A. P. was supported by grants RFBR-08-02-00856-a and RFBR-08-02-92499-a.

[1] F. Sannino, arXiv:0804.0182.
[2] C. T. Hill and E. H. Simmons, Phys. Rep. **381**, 235 (2003); **390**, 553(E) (2004).
[3] F. Sannino and K. Tuominen, Phys. Rev. D **71**, 051901 (2005).
[4] D. D. Dietrich and F. Sannino, Phys. Rev. D **75**, 085018 (2007).
[5] T. A. Ryttov and F. Sannino, Phys. Rev. D **76**, 105004 (2007).
[6] T. A. Ryttov and F. Sannino, Phys. Rev. D **78**, 065001 (2008).
[7] D. D. Dietrich, F. Sannino, and K. Tuominen, Phys. Rev. D **72**, 055001 (2005).
[8] B. Holdom, Phys. Rev. D **24**, 1441 (1981).
[9] B. Holdom, Phys. Lett. B **150**, 301 (1985).
[10] E. Eichten and K. D. Lane, Phys. Lett. B **90**, 125 (1980).
[11] K. D. Lane and E. Eichten, Phys. Lett. B **222**, 274 (1989).
[12] D. K. Hong, S. D. H. Hsu, and F. Sannino, Phys. Lett. B **597**, 89 (2004).
[13] R. Foadi, M. T. Frandsen, T. A. Ryttov, and F. Sannino, Phys. Rev. D **76**, 055005 (2007).
[14] R. Foadi, M. T. Frandsen, and F. Sannino, Phys. Rev. D **77**, 097702 (2008).
[15] S. Catterall and F. Sannino, Phys. Rev. D **76**, 034504 (2007).
[16] S. Catterall, J. Giedt, F. Sannino, and J. Schneible, J. High Energy Phys. 11 (2008) 009.
[17] Y. Shamir, B. Svetitsky, and T. DeGrand, Phys. Rev. D **78**, 031502 (2008).
[18] L. Del Debbio, A. Patella, and C. Pica, arXiv:0805.2058.
[19] L. Del Debbio, M. T. Frandsen, H. Panagopoulos, and F. Sannino, J. High Energy Phys. 06 (2008) 007.
[20] J. M. Cline, M. Järvinen, and F. Sannino, Phys. Rev. D **78**, 075027 (2008).
[21] The technibaryon number is assumed to be broken via new interactions beyond the electroweak sector.
[22] T. Appelquist and F. Sannino, Phys. Rev. D **59**, 067702 (1999).
[23] R. Foadi and F. Sannino, Phys. Rev. D **78**, 037701 (2008).
[24] T. Appelquist, P. S. Rodrigues da Silva, and F. Sannino, Phys. Rev. D **60**, 116007 (1999).
[25] In Ref. [13], where the chiral symmetry is SU(4), there is an additional term whose coefficient is labeled r_1. With an SU(N) $\times$ SU(N) chiral symmetry this term is just identical to the s term.
[26] M. Bando, T. Kugo, S. Uehara, K. Yamawaki, and T. Yanagida, Phys. Rev. Lett. **54**, 1215 (1985).
[27] M. Bando, T. Kugo, and K. Yamawaki, Phys. Rep. **164**, 217 (1988).
[28] R. Casalbuoni, A. Deandrea, S. De Curtis, D. Dominici, R. Gatto, and M. Grazzini, Phys. Rev. D **53**, 5201 (1996).
[29] The lepton sector works out in a similar way, the only difference being the possible presence of Majorana neutrinos.
[30] R. Sundrum and S. D. H. Hsu, Nucl. Phys. **B391**, 127 (1993).
[31] M. Kurachi and R. Shrock, Phys. Rev. D **74**, 056003 (2006).
[32] R. Barbieri, A. Pomarol, R. Rattazzi, and A. Strumia, Nucl. Phys. **B703**, 127 (2004).
[33] The information on the spectrum alone is not sufficient to constrain s, but it can be measured studying other physical processes.
[34] CDF II Exotics Group Public Page, http://www-cdf.fnal.gov/physics/exotic/exotic.html, Note CDF/PUB/EXOTIC/PUBLIC/9160.
[35] A. Pukhov, arXiv:hep-ph/0412191.
[36] A. Semenov, arXiv:0805.0555.
[37] R. Casalbuoni, S. De Curtis, and M. Redi, Eur. Phys. J. C **18**, 65 (2000).
[38] A. Birkedal, K. T. Matchev, and M. Perelstein, *In the Proceedings of 2005 International Linear Collider Workshop (LCWS 2005), Stanford, California, 2005*, pp. 0314 (unpublished).
[39] H. J. He *et al.*, Phys. Rev. D **78**, 031701 (2008).
[40] A. R. Zerwekh, Eur. Phys. J. C **46**, 791 (2006).
[41] G. L. Bayatian *et al.* (CMS Collaboration), J. Phys. G **34**, 995 (2007).
[42] ATLAS Detector and Physics Performance Technical Design Report, CERN/LHCC/99-14/15, 1999.
[43] G. Brooijmans *et al.*, arXiv:0802.3715.
[44] J. Bagger *et al.*, Phys. Rev. D **52**, 3878 (1995).
[45] O. Kaymakcalan and J. Schechter, Phys. Rev. D **31**, 1109 (1985).
[46] R. S. Chivukula and E. H. Simmons, Phys. Rev. D **78**, 077701 (2008).